

MATERIALS SCIENCE

Local chemical order enables an ultrastrong and ductile high-entropy alloy in a cryogenic environment

Lifang Sun^{1†}, Zhufeng He^{1†}, Nan Jia^{1*}, Yanxin Guo¹, Shuang Jiang², Yuliang Yang¹, Yuxin Liu¹, Xianjun Guan³, Yongfeng Shen^{4*}, Hai-Le Yan^{1*}, Peter K. Liaw⁵

Owing to superior strength-ductility combination and great potential for applications in extreme conditions, high-entropy alloys (HEAs) with the face-centered cubic (FCC) structure have drawn enormous attention. However, the FCC structure limits yield strength and makes the alloys unable to meet ever-increasing demands for exploring the universe. Here, we report a strategy to obtain FCC materials with outstanding mechanical properties in both ambient and cryogenic environments, via exploiting dynamic development of the interstitial-driven local chemical order (LCO). Dense laths composed of the multiscaled LCO domains evolve from planar-slip bands that form in the prior thermomechanical processing, contributing to ultrahigh yield strengths over a wide temperature range. During cryogenic tensile deformation, LCO further develops and promotes remarkable dislocation cross-slip. Together with the deformation-driven transformation and twinning, these factors lead to satisfactory work hardening. The cryogenic loading-promoted LCO, also revealed by ab initio calculations, opens an avenue for designing advanced cryogenic materials.

INTRODUCTION

With the development of science and technology, nowadays, human beings have an ever-increasing demand for exploring the universe. For structural materials applied in high-tech fields, such as aerospace, deep sea, polar-region research, and cryogenic storage, usually both high strength and good ductility in a wide temperature range from ambient to cryogenic temperatures (70 to 298 K) are required. Compared to traditional materials for cryogenic use, high-entropy alloys (HEAs) and medium-entropy alloys (MEAs) with the face-centered cubic (FCC) structure exhibit superior mechanical properties, including high yield strength and remarkable fracture toughness at liquid-nitrogen temperature (77 K) (1–3). Moreover, owing to their excellent strength and ductility combination at room temperature, corrosion, and radiation resistance, this group of alloys has attracted enormous attention (4–10).

Gludovatz *et al.* (1) first reported the superior combination of strength and ductility in an equiatomic FeMnCoCrNi HEA (the Cantor alloy) with the FCC structure at 77 K than that at ambient temperature, which was attributed to a transition of deformation mechanisms from planar-slip dislocation activity at ambient temperature to mechanical nanotwinning with decreasing temperature, i.e., the activation of the twinning-induced plasticity (TWIP) effect. On the basis of that, an ultrafine-grained Cantor alloy with the yield strength and uniform elongation of 798 MPa and 26% at ambient temperature was developed (11). When deformed at 77 K, the alloy also exhibited a superior combination of high yield strength (~1.24 GPa)

and good uniform elongation (~41%). However, the existing FCC-structured HEAs are still unable to provide high yield strengths and decent uniform elongations at ambient and cryogenic temperatures simultaneously, which limits their applications as the key engineering components.

On the other hand, the content of Ni in conventional cryogenic alloys, such as austenitic stainless steels and invar alloys, is usually above 8 atomic percent (at %) (12, 13). Because of the continuously increasing price of Ni in recent years, the development of ultrastrong and ductile but Ni-free alloys for cryogenic use has become an urgent issue. By removing Ni from the Cantor alloy and modifying the proportions of Fe and Mn, Li *et al.* (14) developed a metastable dual-phase [i.e., FCC plus hexagonal close-packed (HCP)] FeMnCoCr HEA in which the stacking fault energy (SFE) has been lowered. A fully recrystallized (RX) $\text{Fe}_{50}\text{Mn}_{30}\text{Co}_{10}\text{Cr}_{10}$ alloy showed the yield strength of 330 MPa and the uniform elongation of 60%, with the joint activation of TWIP, transformation-induced plasticity (TRIP), and bidirectional-TRIP (B-TRIP) effects (15). To further improve strength of the FeMnCoCr-based HEAs in a wide temperature range, solid solutions with the introduction of interstitial atoms were attempted (16–18). For example, He *et al.* (19) obtained ultrastrong and ductile FCC materials for cryogenic applications by doping N and thus tailoring the SFE, but their yield strength at ambient temperature was below 500 MPa, implying that the interstitial alloy still lacked good performances throughout the large temperature range.

Recently, local chemical order (LCO), as a strategy for strengthening MEAs and HEAs, has received widespread attention (20–25). According to the different dimensions, LCO can be classified as short-range order (SRO; below 1 nm) and medium-range order (MRO, 1 to 5 nm) and both play a major role in influencing micromechanical behaviors and elevating strength/hardness of alloys (26–31). Inspired by this, here, we develop a $\text{Fe}_{49}\text{Mn}_{30}\text{Co}_{10}\text{Cr}_{10}\text{N}_1$ (at %) HEA with ultrahigh strength and satisfactory ductility at the ambient-to-cryogenic temperature range, by combining the concept of interstitial-driven LCO strengthening and phase metastability. The material shows a heterostructure with an inhomogeneous distribution of

Copyright © 2024 The Authors, some rights reserved; exclusive licensee American Association for the Advancement of Science. No claim to original U.S. Government Works. Distributed under a Creative Commons Attribution NonCommercial License 4.0 (CC BY-NC).

¹Key Laboratory for Anisotropy and Texture of Materials (Ministry of Education), School of Material Science and Engineering, Northeastern University, Shenyang 110819, China. ²Key Laboratory of Electromagnetic Processing of Materials (Ministry of Education), School of Material Science and Engineering, Northeastern University, Shenyang 110819, China. ³Shi-changxu Innovation Center for Advanced Materials, Institute of Metal Research, Chinese Academy of Sciences, Shenyang 110016, China. ⁴State Key Lab Rolling & Automat, Northeastern University, Shenyang 110819, China. ⁵Department of Materials Science and Engineering, University of Tennessee, Knoxville, TN 37996, USA.

*Corresponding author. Email: jian@atm.neu.edu.cn (N.J.); shenyf@smm.neu.edu.cn (Y.S.); yanhaile@mail.neu.edu.cn (H.-L.Y.)

†These authors contributed equally to this work.

chemical compositions due to the formation of multiscaled LCO structures and a nonuniform distribution of grain sizes caused by partial recrystallization. A novel deformation mechanism involving the development of LCO during plastic deformation proves to be very effective in obtaining ultrastrong and ductile FCC materials, as LCO domains with the enlarged dimensions strengthen the alloy and change the slip mode of dislocations from planar to wavy slips. These findings provide the fundamental understanding of the strengthening induced by the dynamic evolution of LCO and shed light on the design of high-performance FCC materials at ambient-to-cryogenic temperatures.

RESULTS

Mechanical properties

Uniaxial tensile tests were performed on the $\text{Fe}_{49}\text{Mn}_{30}\text{Co}_{10}\text{Cr}_{10}\text{N}_1$ alloy in the partially RX (PRX) and the fully RX (FRX) states (denoted as N1-PRX and N1-FRX materials) at 298 and 77 K, respectively. The engineering stress-strain curves are shown in Fig. 1A in which the mechanical behaviors of the N0-FRX material are also given for comparison. The detailed mechanical properties of the various materials are summarized in table S1. Compared with the $\text{Fe}_{50}\text{Mn}_{30}\text{Co}_{10}\text{Cr}_{10}$ alloy in the FRX state (N0-FRX material), yield strength and tensile strength of the N1-FRX material substantially increase at both 298 and 77 K, indicating that the addition of

interstitial N atoms has a remarkable strengthening effect (32). Unlike the notable ductility loss of the N1-FRX material at cryogenic temperature, strength and ductility of the N1-PRX material have been simultaneously improved at 77 K compared to that at ambient temperature, with the ultrahigh yield strength of 1836 MPa, ultimate tensile strength of 2048 MPa and uniform elongation of 11.6%. These values are higher than that at 298 K (i.e., 1170 MPa, 1224 MPa, and 8.2%). Figure 1B shows work-hardening curves with respect to the true strain of the studied materials, and fig. S1 shows true stress-strain curves, respectively. The results indicate that both N1-PRX and N1-FRX materials exhibit a higher work-hardening capacity during cryogenic deformation, compared to that at ambient temperature. In addition, the work-hardening rates of the N1-PRX material are lower than that of the N1-FRX material at both ambient and cryogenic temperatures, which is a typical feature of ultrafine-grained materials and metals and alloys in the PRX state (33, 34). It is worth noting that work-hardening curves of both N1-FRX and N1-PRX materials exhibit severe serrations during cryogenic deformation, and the fluctuating work-hardening rates even jump to be above 4 and 3 GPa, respectively. This feature may be attributed to the increased lattice friction relevant to the cryogenic temperature and the dynamic strain aging caused by interstitial N atoms (35). We also note that the difference in work-hardening rates of the two materials at 77 K is much lower than that at 298 K, i.e., the difference in work-hardening rates during ambient-temperature deformation at a 0.1

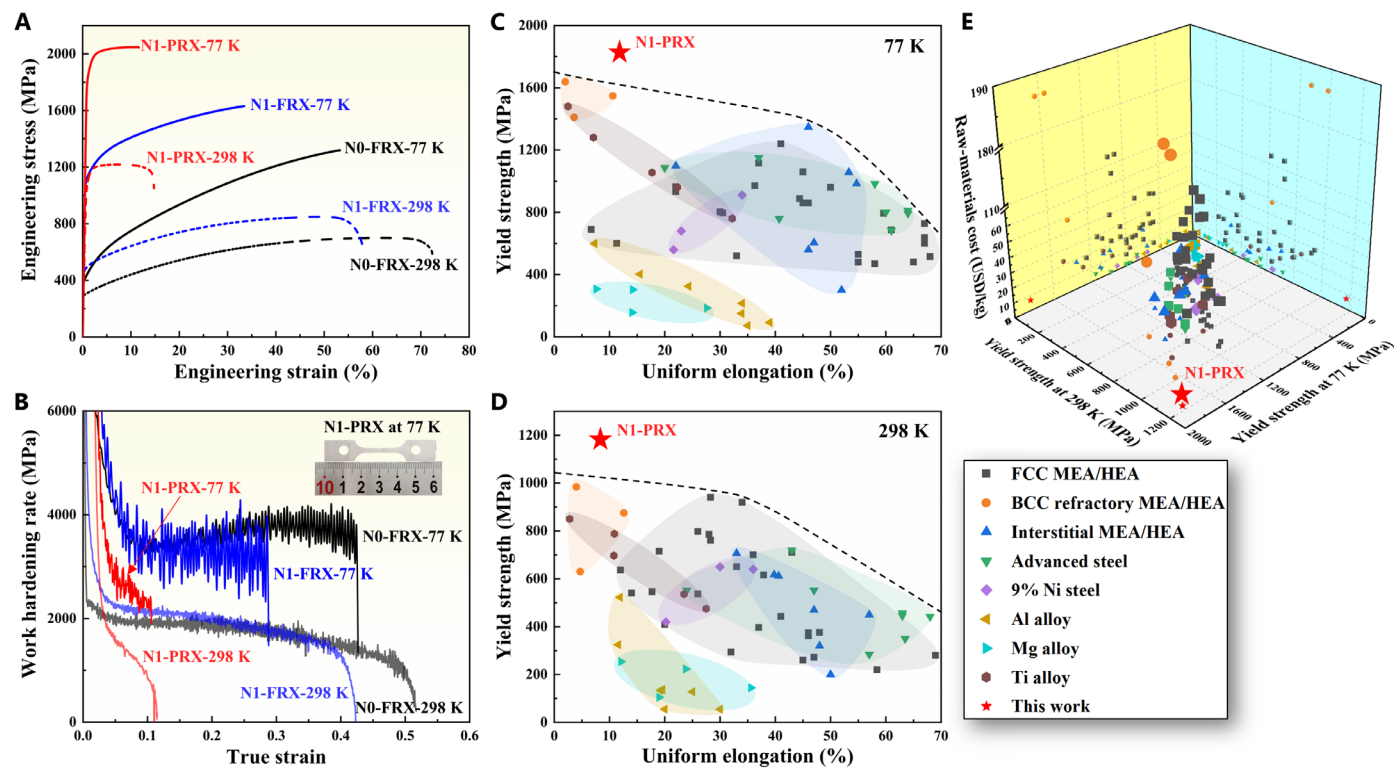


Fig. 1. Mechanical properties of the developed alloy at various states. (A) Engineering stress-strain curves and (B) work-hardening rates with respect to the true strain of the N1 ($\text{Fe}_{49}\text{Mn}_{30}\text{Co}_{10}\text{Cr}_{10}\text{N}_1$) and N0 ($\text{Fe}_{50}\text{Mn}_{30}\text{Co}_{10}\text{Cr}_{10}$) alloys in various states deformed at 298 and 77 K. The inset in (B) shows the N1-PRX material after tensile testing at 77 K. (C and D) Comparison of yield strength versus uniform elongation obtained in the current N1-PRX material with the previously reported cryogenic structural materials at 77 and 298 K. (E) Comparison of yield strengths at both 298 and 77 K versus raw-material cost of the above-mentioned materials. To clearly display the data points in the 3D diagram, their projections in three orthogonal directions are displayed. Detailed mechanical properties and raw-material costs of the materials are listed in data S1. PRX, partially recrystallized; FRX, fully recrystallized.

true strain is 1.3 GPa, whereas the difference at 77 K is only 0.8 GPa. That is to say, the work-hardening ability of the N1-PRX material has been improved when deformed in the cryogenic environment, implying that there is an additional work-hardening mechanism of the N1-PRX material at 77 K. The cryogenically deformed N1-PRX material with the uniformly elongated gauge part is shown in the inset of Fig. 1B, indicating the superior strain-hardening ability of the material.

The yield strength and uniform elongation of the N1-PRX material are compared with the previously reported structural alloys for cryogenic applications at 77 and 298 K, as shown in Fig. 1 (C and D, respectively). The present material (marked by the red star) exhibits remarkable advantages over other FCC, body-centered cubic (BCC), and interstitial MEAs/HEAs, 9% [weight % (wt %)] Ni steels, and advanced high-strength steels within the ambient-to-cryogenic temperature range. Moreover, compared to other alloys with high performances at 77 and 298 K, the N1 alloy maintains the much lower raw-material cost, as shown in Fig. 1E.

Initial microstructures

The initial microstructure of the N1-PRX material is presented in Fig. 2A, which shows a heterostructure composed of the non-RX (NRX) zone with dense lamellar structures (Fig. 2A1) and the RX zone embedded in the NRX matrix (Fig. 2A2). The average grain size of the RX zone is 1.6 μm , and the RX fraction is $\sim 20\%$. At both grain boundaries and in the interior of the RX grains, only a small number of Cr-rich precipitates are dispersed (fig. S2). The phase distribution map obtained from electron backscatter diffraction (EBSD) for the material is shown in fig. S3B, indicative of the FCC-single phase. This trend is also consistent with the result obtained by high-energy x-ray diffraction (HEXRD; Fig. 2B).

To explore the dense lamellar structure of the NRX zone, the transmission electron microscopy (TEM) characterization is made for the N1-PRX material, as presented in Fig. 2 (C and D). Abundant recovery twins (36) that are parallel to each other in individual grains appear in the NRX zone (as indicated by the orange arrows), and dense dislocations are entangled between the twins. In addition, LCO laths in two directions are found within one single crystal (Fig. 2D). Selected-area electron diffraction (SAED) patterns taken from the different laths along the $[112]_\gamma$ zone axis are also given in Fig. 2D, showing the extra sharp superlattice reflections at $1/2 \{311\}_\gamma$ positions (as indicated by the yellow arrows) apart from the diffraction spots from the FCC lattice. This trend indicates the MRO structure within the LCO laths. Namely, the laths composed of MRO/SRO domains and FCC lattices evolve from the planar dislocation slip bands that are prominently activated in the prior cold rolling (37). On the basis of the statistical analysis, the mean width of the LCO laths is 54 nm, and the mean spacing between the neighboring laths is 349 nm. The volume fraction of LCO laths is calculated according to the Fullman's volumetric analysis (38), i.e., $N = \frac{1}{\lambda} = \frac{1}{2t} \frac{f}{1-f}$, where λ is the mean laths spacing, t is the width of laths, and f is the volume fraction of laths. Considering that the NRX fraction of the N1-PRX material is about 80%, the volume fraction of LCO laths in this material is $\sim 19\%$. It is also noted that substructures, such as dislocations, stacking faults, and LCO laths, do not appear in the RX zone of the material, as shown in fig. S3C.

Figure 2 (E to H) shows the detailed characterization of the LCO structure inside LCO laths of the N1-PRX material. The high-angle

annular dark-field scanning TEM (STEM-HAADF) image under $[112]_\gamma$ axis and the corresponding fast Fourier transform (FFT) pattern are shown in Fig. 2E. According to the method proposed for characterizing LCO (23), inverse FFT (IFFT) of the $1/2\{311\}_\gamma$ spot (indicated by red circle in the FFT pattern of Fig. 2E) is made, and the atomic aggregates where red dots are located to constitute LCO domains are shown in Fig. 2F. IFFT image of LCO overlaid with the FCC lattice is shown in Fig. 2G, and the inset is the close-up view showing the atomic arrangement characteristics of LCO (indicated by the yellow dotted rectangle) and FCC matrix. It can be observed that the periodic lattice plane of LCO (indicated by the green arrow) exhibits a plane spacing (d_{LCO}) along the $\{311\}_\gamma$ planes that is twice the interplanar spacing (d_{FCC}) of the FCC lattice (indicated by the red arrow). Figure 2H is a superimposed diagram of the annular bright-field (ABF) images corresponding to Fig. 2 (E and F), showing that LCO tends to form around the N atoms (indicated by the blue arrow) in the austenite matrix. Figure 2 (I and J) shows the STEM-HAADF images of the LCO structure in a RX grain of the N1-PRX material, with the inset in Fig. 2I showing the corresponding FFT pattern. The atomic aggregates representing the LCO domains within the RX grain, i.e., the red dots are located, are shown in Fig. 2J. On the basis of the statistical analysis of the IFFT images in more than 100 regions, the average diameters of LCO domains within LCO laths and RX grains are estimated to be 0.52 and 0.31 nm (Fig. 2K), respectively.

Evolution of deformation microstructures at 77 K

To reveal the origin of the excellent mechanical properties of the N1-PRX material in the cryogenic environment, the microstructural evolution during tensile testing at 77 K is characterized systematically. Figure 3 shows the microstructural evolution of the material deformed to different strain levels. The phase distribution maps (Fig. 3, A1 to C1) show that the areal fraction of the ϵ -martensite in the NRX zone increases from 0.7% at the initial stage of deformation ($\epsilon \sim 1\%$) to 6.0% after fracture ($\epsilon \sim 11.6\%$). This trend indicates that the TRIP effect is activated in the cryogenically deformed alloy, which is consistent with the results obtained from HEXRD (fig. S4). The corresponding orientation distribution maps (Fig. 3, A2 to C2) and pole figures obtained from XRD measurements (fig. S5) of the N1-PRX material after cryogenic deformation indicate that the austenite mainly has the $\{110\}$ textures parallel to the normal direction (ND) of the cold-rolled plate, and in the ϵ -martensite, the $\{10\bar{1}2\}$ textures close to the ND are dominant.

It should be noted that the martensitic transformation in the N1-PRX material under cryogenic deformation is not evident. This feature indicates that except for the TRIP effect, the ultrahigh yield strength and good work-hardening ability should also come from other microstructural configurations, such as dislocations, twins, and/or LCO laths. Therefore, TEM was used to further characterize the microstructure of the N1-PRX material under cryogenic deformation. Detailed observations of the material at the initial stage of deformation ($\epsilon \sim 1\%$) have shown that dislocations, stacking faults, deformation twins, and ϵ -martensite laths are formed in both RX and NRX zones (fig. S6). Dark-field images of deformation twins and ϵ -martensite laths in the NRX zone show that the mean width and spacing of deformation twins are 29 and 276 nm, and those of ϵ -martensite laths are 11 and 426 nm, respectively. In the RX zone, the

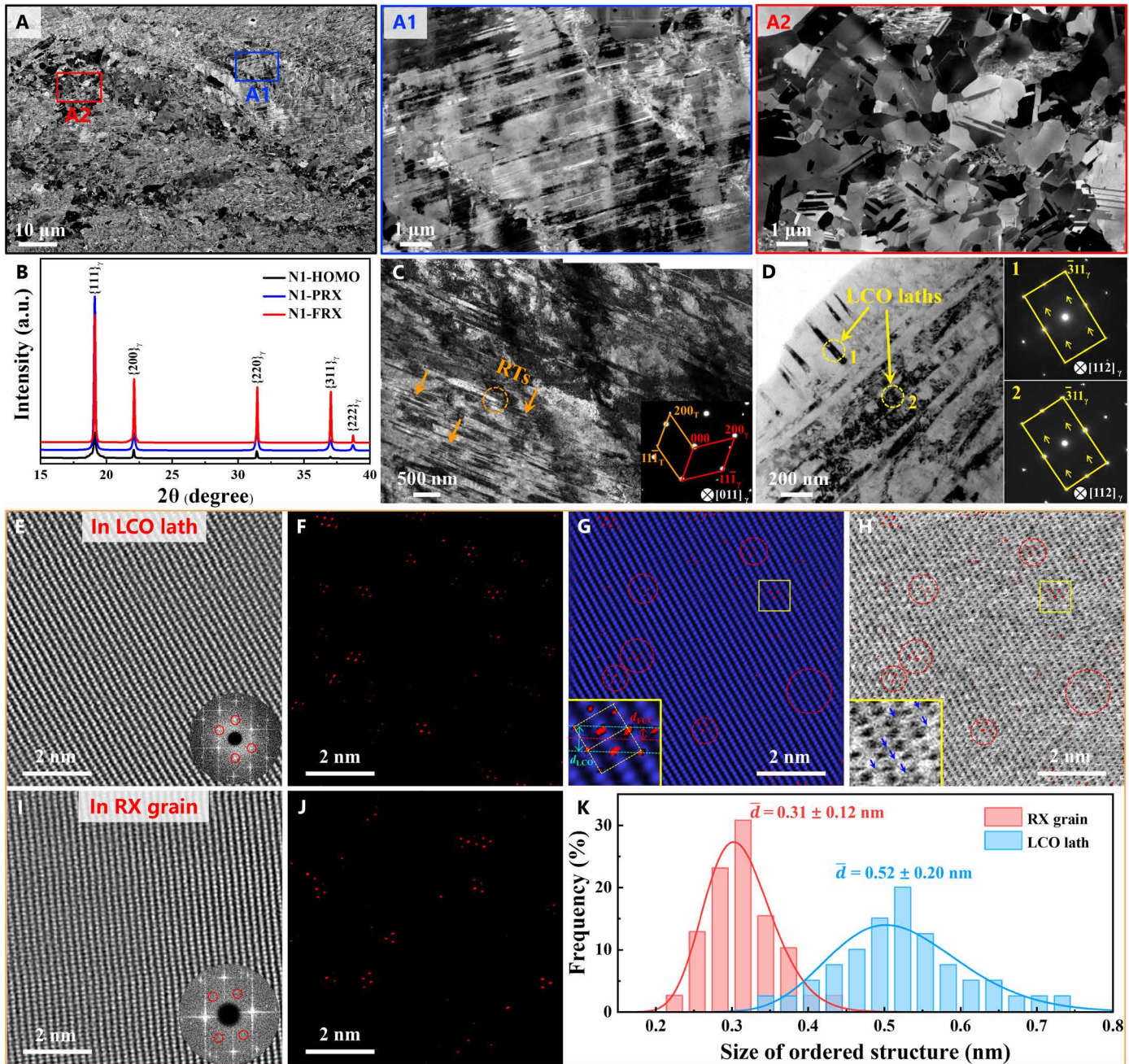


Fig. 2. Microstructures of the N1-PRX material before tensile testing. (A) BSE micrograph obtained from the longitudinal section (RD-ND plane) of the material. (A1 and A2) The magnified views of the NRX and the RX zones in (A). (B) XRD patterns of the N1 alloy in various states. (C) TEM micrographs of parallel recovery twins indicated by orange arrows and the diffraction pattern taken from the orange dotted circle. (D) TEM micrograph of the LCO laths with different directions and the SAED patterns taken from the different lath bundles along the $[112]_{\gamma}$ zone axis. (E) STEM-HAADF image along the $[112]_{\gamma}$ axis taken from a LCO lath in the NRX zone and the corresponding FFT pattern with sharp spots at $1/2\{311\}_{\gamma}$. (F) IFFT image showing LCO domains in the LCO lath. (G) IFFT image of LCO domains overlaid with FCC lattice. The inset is the close-up view of a LCO domain taken from the yellow solid rectangle. Some domains with the larger dimensions are indicated by red dotted circles. (H) IFFT image of LCO overlaid with the ABF image corresponding to (E). The close-up view taken from the yellow solid rectangle shows the distribution of interstitial N atoms (indicated by blue arrows). (I) STEM-HAADF image along the $[112]_{\gamma}$ axis taken from the interior of one RX grain and the corresponding FFT pattern with diffuse scattering. (J) IFFT image showing LCO domains in the RX grain. (K) Size distribution of LCO domains in LCO laths and RX grains of the material. RT, recovery twin.

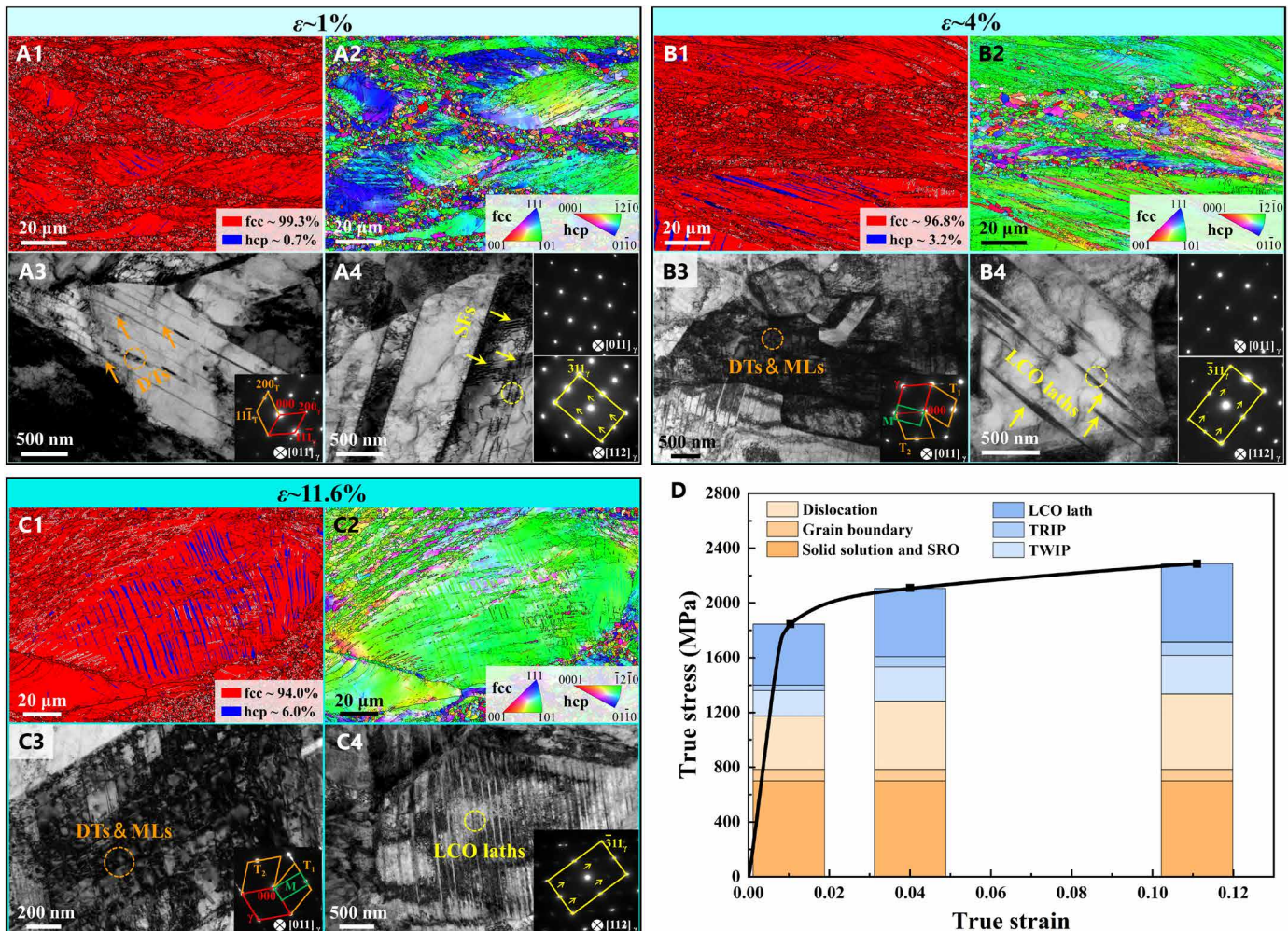


Fig. 3. Microstructure evolution of the N1-PRX material during deformation at 77 K. (A1 to C1) Phase distribution maps and (A2 to C2) orientation maps showing grain-orientation distributions relative to ND. The horizontal direction in the EBSD maps is parallel to the tensile axis. (A3 to C3) TEM images show that microstructures are refined by ϵ -martensite laths and deformation twins in the RX zone at (A) 1%, (B) 4%, and (C) 11.6% strains, respectively. The insets in (A3) to (C3) are the corresponding diffraction patterns taken from the orange-dotted circles. (A4) Dense stacking faults and (B4) LCO laths are indicated by the yellow arrows in one RX grain and the corresponding SAED patterns along the $[011]_y$ and $[112]_y$ zone axes. (C4) Dense LCO laths in one RX grain and the diffraction pattern along the $[112]_y$ zone axis taken from the yellow dotted circle. (D) Various strength contributions to the flow stress of the N1-PRX material during tensile testing at 77 K. In the phase distribution maps, high-angle boundaries with misorientation angles larger than 10° are indicated by thick black lines, low-angle boundaries with misorientation angles between 3° and 10° are indicated by thin black lines, and $\Sigma 3$ twin boundaries in the FCC phase are represented by white solid lines, respectively. DT, deformation twin; ML, martensite lath; SF, stacking fault.

mean width and spacing of deformation twins are 15 and 195 nm, and those of ϵ -martensite laths are 7 and 388 nm, respectively.

On the basis of the twin-nucleation model proposed by Mahajan *et al.* (39) and a crystal plasticity model for simulating the deformation-induced HCP phase transformation (40), the critical stress required for the twin formation and growth of the ϵ -martensite nucleus for the N1 alloy at different temperatures are calculated (section S1). The critical stresses for activating mechanical twinning are 421 to 438 MPa and 318 to 335 MPa in this N-doped alloy when deformed at 298 and 77 K, respectively, and those for the growth of HCP nucleus are 502 to 507 MPa and 549 to 553 MPa at the corresponding temperatures. To verify the theoretical calculation mentioned above, we loaded the N1-PRX material to 1000 MPa at 298 K and 1700 MPa at 77 K. The TEM results (fig. S7) show that twinning occurs at

298 K, and both twinning and martensitic transformation occur at 77 K before yielding, respectively. The microstructure of the alloy is then refined, which is consistent with the TEM observation at the initial stage of plastic deformation (fig. S6, $\varepsilon \sim 1\%$). The morphologies of dislocations and nanotwins in the RX grains can be clearly discerned, indicating that the N1-PRX material is in a low strain state (Fig. 3A3). Since it is impossible to distinguish whether LCO laths in the NRX zone are formed during cold rolling or the subsequent cryogenic tensile loading, we next focus on microstructures inside the LCO laths within the RX zone, so as to reveal the evolution of the laths during plastic deformation.

At the initial stage of deformation, extensive planar slip is identified in the RX zone (Fig. 3A4). The SAED pattern of the slip-banded region along the $[112]_y$ axis shows an extra diffuse scattering at the

$1/2 \{311\}_{\gamma}$ positions, which indicates that the LCO structures featured with SRO also exist in this region. The TEM observations of the N1-PRX material at a strain of 4% during cryogenic deformation are shown in Fig. 3B and fig. S8, in which stacking faults, planar-slip bands, and LCO laths are extensively observed in both RX and NRX zones. The SAED patterns of LCO laths in the RX zone along $[112]_{\gamma}$ and $[011]_{\gamma}$ axes are presented in Fig. 3B4, showing the characteristics of LCO and stacking faults simultaneously. Combined with Fig. 3A4, it is known that the density of planar-slip bands and the dimension of LCO structures in the N1-PRX material increase synchronously with deformation, indicating that the LCO laths are evolved from planar-slip bands promoted by the interaction between the interstitial-driven multiscaled LCO and dislocations. The mean width and spacing of LCO laths in the RX zone are 15 and 435 nm, respectively, and the volume fraction of the laths within this zone is 6%. Moreover, the dense deformation twins and ϵ -martensite laths are formed in both NRX and RX zones (fig. S8, A and B), and secondary twins are also found in some RX grains (Fig. 3B3), leading to the further refinement of the microstructure. Statistical analysis of TEM observations has shown that in the NRX zone, the mean width and spacing of deformation twins are 34 and 240 nm, and those of ϵ -martensite laths are 15 and 352 nm, respectively. In the RX zone, the mean width and spacing of twins are 17 and 175 nm, and those of ϵ -martensite laths are 10 and 285 nm, respectively.

The TEM micrographs of a region close to the fracture surface of the N1-PRX material deformed at 77 K ($\epsilon \sim 11.6\%$) are shown in Fig. 3 (C3 and C4) and fig. S9. It is clearly seen that LCO laths become denser in the RX zone, with the average width and spacing of 22 and 389 nm, respectively. The volume fraction of LCO laths in the RX zone reaches 10% at this stage, which is higher than that at a 4% strain (Fig. 3B4). High-resolution TEM images of the LCO structure in RX grains and LCO laths of the N1-PRX material deformed at 77 K ($\epsilon \sim 11.6\%$) are shown in fig. S10 (A and C, respectively), and the insets are the corresponding FFT patterns. The atomic aggregates representing LCO domains within RX grains and LCO laths are shown in fig. S10 (B and D), and in the LCO laths, some domains indicated by blue dotted circles with diameters larger than 1 nm are identified as MRO structures. On the basis of the statistical analysis of the IFFT images in different regions, the average diameters of LCO in RX grains and LCO laths are estimated to be 0.51 and 0.72 nm, respectively (fig. S10K). Compared to the N1-PRX material before deformation, the mean diameter of LCO domains in the RX grains increases from 0.31 to 0.51 nm after deformation at 77 K, indicating that the LCO domains evolve during deformation and finally form the laths. Meanwhile, dense deformation twins and ϵ -martensitic laths still exist in both NRX and RX zones (fig. S9, A and B). In the NRX zone, the mean width and spacing of deformation twins are 35 and 223 nm, and those of ϵ -martensite laths are 17 and 317 nm, respectively. In the RX zone, the mean width and spacing of deformation twins are 18 and 164 nm, and those of ϵ -martensite laths are 10 and 234 nm, respectively. The structural parameters (mean width, spacing, and volume fraction) of LCO lath, deformation twin, and ϵ -martensite in both NRX and RX zones of the material at different strains have been summarized in table S3. According to the statistical information on these deformation configurations, microstructures of both NRX and RX zones in the N1-PRX material have been remarkably refined at the early stage of cryogenic deformation ($\epsilon \leq 4\%$). However, as the applied strain further increases to 11.6%, both TWIP and TRIP effects become indistinctive.

DISCUSSION

Origin of ultrahigh yield strength in the N1-PRX material at cryogenic temperature

The N1-PRX material shows an excellent combination of yield strength and uniform elongation at both ambient and cryogenic temperatures. Compared with that at 298 K, both the yield strength and uniform elongation of the alloy have been improved. According to our previous study (19), the N1-PRX material exhibits a high yield strength of 1078 MPa at 77 K, which is mainly due to the microstructure refinement caused by the activation of athermal martensitic transformation and mechanical twinning in the elastic regime. Here, the cryogenic yield strength of the N1-PRX material is further elevated by 758 MPa, which is considered to be related to its specified lamellar structure (Fig. 2A1). This mainly includes dense recovery twins and LCO laths in the NRX zone (Fig. 2, C and D), as the deformation-induced martensite is not prevalent in the cryogenically deformed N1-PRX material. Those twins and LCO laths are formed in the cold-rolling process and retained after the subsequent annealing.

On the basis of the initial microstructure of the material, the origin of strengthening at the cryogenic temperature is summarized as solid-solution strengthening (σ_S , considered as the summation of the strengthening caused by the solid solution and lattice friction at low temperature), the SRO-induced strengthening (σ_{SRO}), dislocation strengthening (σ_D), grain-boundary strengthening (σ_G), the TWIP effect induced strengthening (σ_{TWIP}), the TRIP effect-induced strengthening (σ_{TRIP}), and the LCO lath-induced strengthening ($\sigma_{LCO\ lath}$), i.e., $\sigma_{0.2}(77\text{ K}) = \sigma_S + \sigma_{SRO} + \sigma_D + \sigma_G + \sigma_{TWIP} + \sigma_{TRIP} + \sigma_{LCO\ lath}$. First, the dislocation density of the N1-PRX material is calculated to be $7.13 \times 10^{14} \text{ m}^{-2}$ with the modified Williamson Hall method (41). Then, σ_D at 298 and 77 K are calculated as 322 and 377 MPa, respectively, and σ_G is 83 MPa based on the Hall-Petch relationship. The summation of σ_S and σ_{SRO} at 77 K is calculated as 701 MPa, and σ_{TWIP} and σ_{TRIP} are determined as 186 and 41 MPa, respectively. Last, the contributions of $\sigma_{LCO\ lath\ boundary}$ and $\sigma_{LCO\ inside\ lath}$ in the material are 183 and 265 MPa, respectively. The detailed calculation process can be found in section S2. The ϵ -martensitic transformation is not activated in the N1-PRX material during deformation at 298 K (figs. S4 and S7), and then $(\sigma_S + \sigma_{SRO})$ and σ_{TWIP} at ambient temperature are determined as 298 and 19 MPa, respectively. The contributions of the various mechanisms in the N1-PRX material at two temperatures are exhibited in fig. S11B, which indicates that the extraordinary yield strength of the material in the wide temperature range primarily originates from the LCO lath-induced strengthening (~448 MPa). In addition, the elevation of yield strength at the cryogenic temperature compared with at ambient temperature is owing to the dynamic Hall-Petch effect contributed by σ_{TWIP} , σ_{TRIP} , and the increased σ_f in the cryogenic environment (42). This is calculated as the difference in the summation of $\sigma_S + \sigma_{SRO}$, σ_{TWIP} , and σ_{TRIP} at the different temperatures, i.e., 611 MPa.

In the above discussion, the total strength is calculated as the summation of various strengthening contributions. However, it should be made clear that such an assumption may not be accurate for MEAs and HEAs, because the matrix in those alloys is actually in a “whole-solute” state without a well-defined solute, and the strengthening mechanisms may depend on each other (37, 43, 44). That is to say, the calculated strengthening contributions in the present materials can only be used for roughly estimating different contributions from the multiple strengthening mechanisms.

Evolution of LCO laths and its influence on deformation behavior

To further explore the evolution of LCO laths and their influence on micromechanical behavior of the studied HEA during cryogenic loading, the formation and dynamic evolution of the laths in the RX zone of the N1-PRX material are traced. Figure 3 (A4 to C4) shows detailed observations for the RX zone in the material at 1, 4, and 11.6% strains under 77 K, respectively. At the initial stage of deformation ($\epsilon \sim 1\%$), abundant nanotwins and stacking faults are formed in the RX grains (Fig. 3, A3 and A4). Dense dislocations are blocked at twin boundaries and grain boundaries, and dislocation interaction and entanglement occur at the stacking faults (fig. S12, A and B). At this stage, LCO laths have not been formed. When the applied strain reaches 4%, the laths are evolved from planar-slip bands, which are facilitated by the interaction between the multiscaled LCO structures and dislocations, and the density of LCO laths increases with deformation. In the N1-FRX material composed of FRX grains, LCO laths also develop with deformation at 77 K, as presented in fig. S13. Our ab initio calculations have indicated that in the FeMnCoCr-based HEA, Fe and Co atoms tend to occupy the same atomic site together, while Mn and Cr atoms prefer to reside at another site (fig. S14). To further understand the promoted dynamic development of LCO under the cryogenic environment, the temperature-dependent Gibbs free energy of the FCC configuration and one specified LCO configuration (i.e., $[Fe_{0.4}Co_{0.1}]_a[Mn_{0.3}Cr_{0.1}Fe_{0.1}]_b$) are calculated. Furthermore, the effect of strain on the formation of LCO is examined by evaluating the evolution of Gibbs energy under simple shear along $(111)[1\bar{1}\bar{2}]$ (Fig. 4A). Figure 4B shows the free energy difference ($\Delta G_{FCC \rightarrow LCO}$) between the LCO and FCC configurations as a function of temperature, in which both conditions with and without straining are given. Compared with 300 K, the configuration featured with LCO at 77 K is more stable with the much lower free energy. Moreover, at both temperatures, the stability of the LCO configuration increases as the external strain is applied. These agree well with the substantially developed LCO laths observed in the alloy during cryogenic tensile deformation (Fig. 3, A4 to C4).

Different degrees of LCO in HEAs may also lead to specific dislocation behaviors that are different from traditional alloys. As the

dimension of LCO increases, the possibilities of interactions between LCO structures and dislocations, dislocation accumulation and cross-slip increase, and the mechanical properties of bulk HEAs are changed (45–47). Dislocations in the RX zone of the N1-PRX material during the cryogenic deformation are characterized. At the initial stage of deformation ($\epsilon \sim 1\%$), planar slip occurs in the RX grains (indicated by the red dotted lines in fig. S12A), and slip bands preferentially form at grain boundaries and extend towards the interior of grains. In addition, a large number of wavy dislocation lines are generated, and dislocation entanglements appear near the planar-slip dislocation arrays (fig. S12, A and B). As the strain increases to 4%, profuse fine twins and secondary twins are found, and dense dislocations are accumulated between the neighboring twins. Meanwhile, abundant stacking faults (indicated by the yellow arrows) and planar-slip bands (indicated by the blue arrows) are formed, as shown in fig. S8C. The detailed characterization of dislocations in the RX grains is given in fig. S12 (C and D), showing that cross-slip (indicated by green arrows) and dislocation entanglements (indicated by yellow arrows) occur frequently near the slip bands and stacking faults. Moreover, both straight and curved cross-slip dislocation lines are observed, because some arcuate dislocations formed due to local shear are restored after the stress release (48). Obviously, cross-slip is more notable as the cryogenic deformation proceeds. At the late stage of deformation ($\epsilon \sim 11.6\%$), the dislocation interaction becomes more intense and dislocation cells form (fig. S12E).

Detailed characterizations of the RX zone in the N1-PRX material during deformation at 77 K are shown in Fig. 5 (A to C). The SAEDs taken from the regions (red circles) without dislocations or stacking faults show that at different stains, no diffuse scattering appears at the $1/2\{311\}_\gamma$ positions along the $[112]_\gamma$ zone axis. For regions with only staking faults, the diffraction patterns taken from the green circles show diffuse scattering at the $1/2\{311\}_\gamma$ positions. The SAEDs taken from the yellow circles where stacking faults intersect with the curved dislocation lines show the sharp scattering at the $1/2\{311\}_\gamma$ positions, as indicated by the yellow arrows. On the basis of the reciprocal relationship between real and reciprocal spaces (49), the change in diffraction patterns in a reciprocal space from

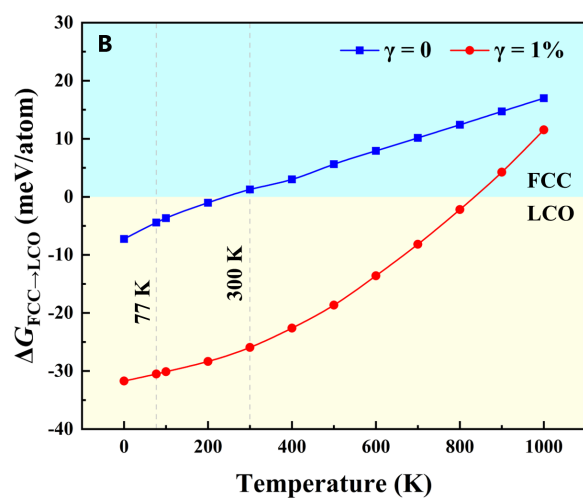
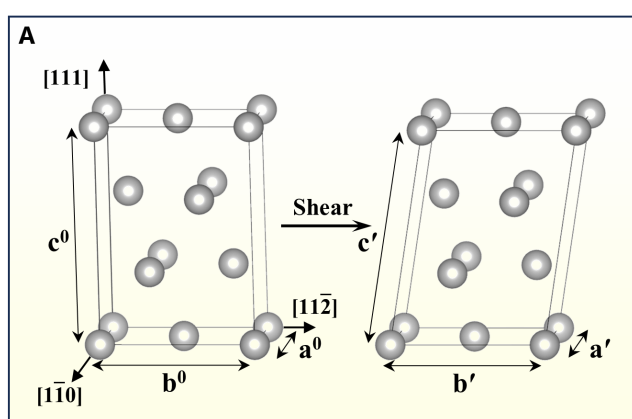


Fig. 4. Gibbs free energy of FeMnCoCr alloy. (A) Shear strain along $(111)[1\bar{1}\bar{2}]$. (B) Difference in Gibbs free energy ($\Delta G_{FCC \rightarrow LCO}$) between the FCC and LCO configurations as a function of temperature.

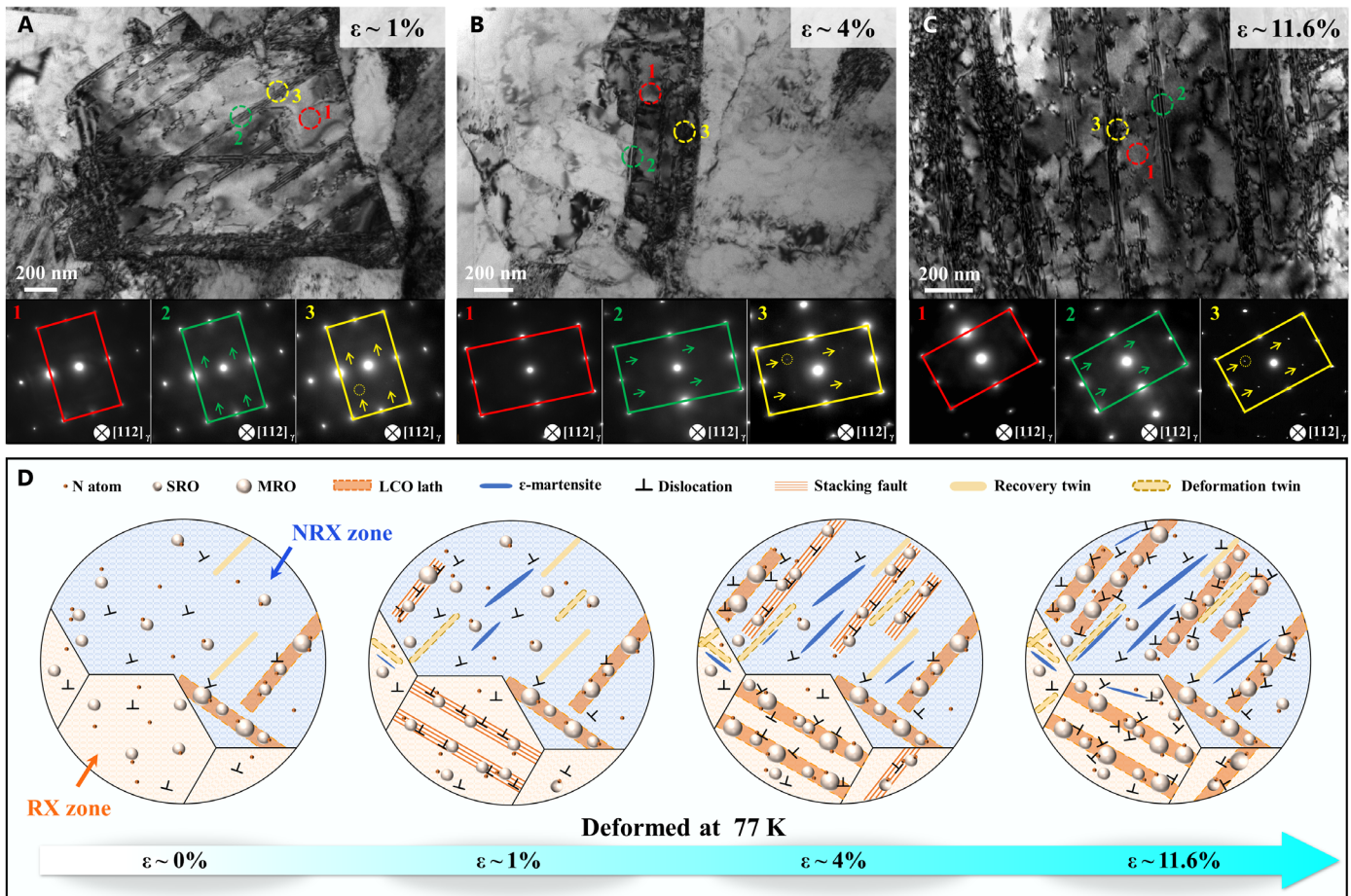


Fig. 5. Microstructures of the N1-PRX material deformed at 77 K with increasing strain. TEM micrographs of the RX zone in the material at (A) $\varepsilon \sim 1\%$, (B) $\varepsilon \sim 4\%$, and (C) $\varepsilon \sim 11.6\%$ strains. The insets in (A) to (C) show corresponding diffraction patterns along the $[112]_\gamma$ zone axis taken from the red, green, and yellow dotted circles, respectively. The regions highlighted by these three circles are typical of the austenitic matrix, the positions of stacking faults without intersecting with dislocations, and the positions where stacking faults intersect with the curved dislocations, respectively. (D) Schematic sketch showing deformation mechanisms in the N1-PRX material under cryogenic tensile loading.

diffuse to sharp scattering is ascribed to the increased LCO dimension. On the basis of the above analysis, the interaction between LCO structures and dislocations can be clarified. Namely, when one LCO structure changes from SRO to MRO, its ability to hinder dislocation slips becomes more notable, thus promoting the occurrence of cross-slip.

SFE is a key factor that determines plastic-deformation mechanisms of the FCC materials (50–52). At 77 K, the SFE of the N1 alloy is -3 to -1 mJ/m² (19). In general, in traditional metals and alloys with such low SFEs, the stress- or strain-induced displacive phase transformation dominates, and dislocations exhibit a notable planar-slip feature. However, in the cryogenic condition, the N1-PRX material displays an indistinctive TRIP effect that is also noted as the sluggish martensitic transformation in a newly developed Fe₃₀Ni₂₀Co₂₀Cr₂₀Si₁₀ (at %) HEA with the ultralow SFE (~ 7 mJ/m²) (53). In addition, abnormal dislocation behavior is found in the present cryogenically deformed material. This feature may be due to the severe lattice distortion caused by the interstitial-driven LCO structures, which leads to the pinning of dislocations and the increased local SFE. The LCO driven by interstitial atoms or large substitutional atoms can cause severe localized lattice

distortion and induce large strain fields around it. These atoms interact with dislocations through the “pinning” effect, which promotes frequent cross-slip of the dislocations during deformation, thus changing the plastic-deformation mechanism (21, 54–57). Moreover, SFE can be substantially influenced by LCO structures. The SFE of MEA/HEA is strongly dependent on its local atomic structures, leading to the varied SFE at different locations, i.e., forming the local SFEs (58). Therefore, the SFE can be regulated within a local region by adjusting the LCO structure, thereby controlling the behavior of dislocations (20, 22). In summary, when the N1-PRX material undergoes plastic deformation at 77 K, planar slip should have been activated in the disordered FCC matrix. However, because of the severe lattice distortion caused by the LCO structures, including both SRO and MRO, within the LCO laths, dislocation motion is hindered. Meanwhile, because of the increased local SFE, cross-slip is promoted in the alloy.

Deformation mechanisms in the metastable and LCO-dominated alloy at 77 K

For the N1-PRX material under 77 K, deformation twins and ϵ -martensite laths have already been formed in both RX and NRX

zones in the initial stage of plastic deformation, and TWIP and TRIP effects become more evident with deformation. The formation of dense lamellar twins and ϵ -martensite laths makes the microstructure dynamically refined, which effectively hinders dislocation motion and contributes to work hardening of the bulk material. Meanwhile, the LCO laths are formed continuously, and the density of the laths increases with deformation. The lath boundaries further refine the microstructure, providing additional work-hardening capability. In addition, because of the lattice distortion caused by the interstitial-driven multiscaled LCO structures and the increase in the local SFE, cross-slip is promoted, which leads to the more complex interaction between dislocations. The activation of cross-slip promotes stress relief and strain nonlocalization to some extent (59, 60), which is beneficial for improving ductility of the alloy.

The strengthening contributions to the flow stress ($\sigma_{\text{flow stress}}$) of the N1-PRX material at strains of 1, 4, and 11.6% under 77 K are quantitatively analyzed. $\sigma_{\text{flow stress}}$ is composed of σ_S , σ_{SRO} , σ_D , σ_G , σ_{TWIP} , σ_{TRIP} , and $\sigma_{\text{LCO lath}}$. First, the dislocation density of the material at 1, 4, and 11.6% strains can be calculated as 7.64×10^{14} , 1.25×10^{15} , and $1.53 \times 10^{15} \text{ m}^{-2}$, respectively. σ_D at the corresponding strains are calculated to be 390, 498, and 551 MPa, respectively. Then, σ_{TWIP} with respect to those strains are predicted as 186, 251, and 283 MPa, and the corresponding σ_{TRIP} are calculated as 41, 75, and 98 MPa, respectively. The $\sigma_{\text{LCO lath}}$ boundary with respect to the three strains are calculated as 183, 208, and 268 MPa, respectively. Last, the σ_{LCO} inside lath at 1, 4, and 11.6% strains are estimated to be 261, 290, and 302 MPa, respectively. The detailed calculation process is given in section S3, and the contributions of various strengthening mechanisms to the flow stress are exhibited in Fig. 3D. The results show that the dynamic Hall-Petch effect composed of deformation twins and ϵ -martensite laths contributes 99 and 55 MPa to the increase of $\sigma_{\text{flow stress}}$ as deformation increases from 1 to 4% and from 4 to 11.6%, respectively. However, $\sigma_{\text{LCO lath}}$ is 54 and 72 MPa at these two stages of straining, which indicates that the TRIP/TWIP effects and the development of LCO laths are dominant deformation mechanisms of the N1-PRX material in the early and the late stages of cryogenic deformation, respectively. Moreover, the marked fluctuation in the work-hardening curves of the studied materials deformed at 77 K is mainly owing to their microstructures frequently refined by the development of twins, martensites, and LCO laths, as well as the softening effect induced by martensite transformation and mechanical twinning (61, 62). In addition, the fluctuation phenomenon is promoted because of the increased lattice-friction resistance relevant to the cryogenic environment together with the more evident dislocation interactions promoted by the formation of multiscaled LCO structures. This trend enables the good work-hardening ability of the N1-PRX material (Fig. 1B).

In the current study, by exploiting an unusual deformation mechanism of the interstitial-driven LCO evolution, we obtained a PRX $\text{Fe}_{49}\text{Mn}_{30}\text{Co}_{10}\text{Cr}_{10}\text{N}_1$ (at %) alloy, i.e., the N1-PRX material with an excellent combination of ultrahigh strength and satisfactory ductility at both ambient and cryogenic temperatures. The microstructure evolution and micromechanical behavior of the material were systematically investigated, based on which the strengthening and toughening mechanisms of bulk alloys were elucidated. First, the ultrahigh yield strengths of the material at both ambient and cryogenic temperatures mainly originate from LCO laths (~448 MPa). Second, the remarkable increase of the yield strength at 77 K, compared to 298 K (~611 MPa), is attributed to the activation of the TRIP

effect and the more evident TWIP effect in the elastic regime as well as the increased lattice friction at the low-environmental temperature. Then, the satisfactory work-hardening ability of the material under 77 K is attributed to the joint activation of planar- and cross-slip of dislocations, TWIP/TRIP effects, and dynamic evolution of LCO laths. Especially, those LCO laths are evolved from planar-slip bands that are prevalent in the cryogenically deformed alloy with an ultralow SFE. To illustrate the cryogenic deformation mechanism of the N1-PRX material, a schematic illustrating the microstructure evolution during tensile loading at 77 K is shown in Fig. 5D. The main deformation mechanism of the material at the early stage of plastic deformation is the combined TRIP and TWIP effects, and that at the late deformation stage is the evolution of LCO laths. Moreover, dislocation activity has been changed with the evolution of LCO laths during cryogenic deformation. The dimension of LCO within the laths increases continuously with deformation, and the evolution of LCO structures from SRO to MRO promotes the activation of cross-slip.

In conclusion, through unraveling evolution of the interstitial-driven LCO laths in a cryogenically deformed FCC alloy, we have verified that the strategy of introducing the dynamically developed LCO is particularly effective for improving the strength and ductility combination of bulk materials. This is because the continuously enlarged LCO domains could strengthen the alloy and change the slip mode of dislocations from the planar to wavy slips. These findings reveal the effect of cryogenic loading on the formation and evolution of LCO structures and the resultant dislocation activities, which guides the development of advanced materials for cryogenic use. Furthermore, the LCO-dominated microstructural design concept can also be extended to more alloy classes, such as advanced steels and BCC MEAs/HEAs, where LCO can be dynamically regulated to have a crucial impact on their mechanical performances.

MATERIALS AND METHODS

Materials preparation

The nominal chemical compositions of the studied alloys are $\text{Fe}_{50}\text{Mn}_{30}\text{Co}_{10}\text{Cr}_{10}$ and $\text{Fe}_{49}\text{Mn}_{30}\text{Co}_{10}\text{Cr}_{10}\text{N}_1$ (at %) HEAs, which are hereafter denoted as N0 and N1 alloys, respectively. The alloys were produced by melting and casting a mixture of pure metals (purity >99.9 wt %) and MnN using a vacuum-induction furnace under Ar atmosphere protection. After hot forging at 1200°C, the alloys underwent hot rolling at 1050°C by several passes to achieve a 50% reduction in total thickness. Then, they were homogenized at 1200°C for 2 hours to obtain the homogenized (HOMO) materials. Last, the homogenized alloys were cold rolled by multiple passes until the reduction reached 60% [denoted as the cold-rolled (CR) state], and then annealed in a salt bath furnace at 700° (below the recrystallization temperature) and 900°C (above the recrystallization temperature) for 3 min, followed by water quenching, to obtain the PRX and the FRX materials, respectively.

Mechanical tests

Dog bone-shaped tensile specimens with a gauge dimension of $15 \times 3 \times 2 \text{ mm}^3$ (length \times width \times thickness) were machined by electrical discharging, followed by mechanical polishing to remove the oxide layers and macrodefects. An Instron 5982 testing apparatus equipped with a cold chamber controlled by liquid nitrogen was used to conduct uniaxial tensile tests at a strain rate of 10^{-3} s^{-1} , and

at least three samples were tested for each material. Shear modulus and Poisson's ratio of the N1 alloy at ambient temperature were measured using a high-temperature elastic modulus tester (RFDA HT1600-DS). Dislocation densities were determined by performing HEXRD measurements using the BL14B1 beamline at the Shanghai Synchrotron Radiation Facility (SSRF). A transmission mode was used as the diffraction geometry, with the incident beam energy of 18 keV ($\lambda = 0.6887 \text{ \AA}$) and the beam size of $300 \times 300 \mu\text{m}^2$. The detailed information on the beamline, BL14B1, can be found in (63).

Microstructure characterization

Microstructures of the studied materials were characterized by a scanning electron microscope (SEM) equipped with the backscatter electron (BSE) detector (Zeiss Ultra Plus). The orientation distribution and phase composition of the N1-PRX material before and after tensile testing were revealed by the SEM equipped with the Oxford HKL EBSD detector (JEOL JSM-7001F). The operating voltage and the step size were 20 kV and 80 nm, respectively. The EBSD data were then postprocessed, using Channel 5 software (Oxford Instruments, London, UK), and more than five different regions were analyzed statistically for each material to determine the phase composition. To obtain a flat surface and remove strain layers, the specimens for EBSD and BSE characterizations were mechanically polished and electro-polished successively. Detailed microstructure evolution before and after tensile deformation was further investigated, using the TEM equipped with an energy-dispersive spectrometer (JEOL JEM-2100F) and the spherical aberration-corrected TEM (JEM-ARM200F) equipped with STEM-HAADF/BF detectors. The TEM samples for TEM were first mechanically polished to a thickness of 50 μm and then thinned with a twin-jet electro-polisher under 25 V and at -25°C . The electrolyte used for electro-polishing and twin-jet electro-polishing was a mixture of 10 vol % HClO_4 and 90 vol % $\text{C}_2\text{H}_5\text{OH}$. To identify the macro-orientation distribution of the specimen after uniaxial tensile testing at 77 K, XRD characterization was performed on a Rigaku Smartlab x-ray diffractometer using the Co-K α radiation with a wavelength of 1.7889 \AA .

Here, the sample coordinate system is defined as three orthogonal directions, namely, the rolling direction (RD), the transverse direction (TD), and the ND of the rolled sheets. The specimens for BSE and EBSD observations were taken from the longitudinal sections (RD-ND planes), and those for XRD, HEXRD, and TEM characterizations were obtained from the RD-TD planes. The positions with the cross-sectional area of 1.99×2.98 , 1.97×2.92 , and $1.88 \times 2.82 \text{ mm}^2$ were selected as the regions corresponding to the cross-sectional area reductions of 1, 4, and 11.6% for the deformed materials, respectively.

Theoretical calculation

The total energies were calculated by an improved screened Korringa-Kohn-Rostoker muffin-tin orbitals method (64, 65). The chemical disorder was treated using the coherent potential approximation (66). The soft-core scheme and the generalized gradient approximation in the Perdew-Burke-Ernzerhof parametrization (67) for the exchange correlation function were adopted. The Green functions for the valence states were calculated for 32 complex energies (68). The muffin-tin basis set included s, p, d, and f orbitals. Using the disordered local moment model, the paramagnetic state of alloys was described (69). The first Brillouin zone was sampled

with $21 \times 21 \times 21$ uniform Monkhorst-Pack k -point meshes for FCC and $13 \times 8 \times 3$ for the LCO structure [see models in fig. S14B (23)]. To model the effect of shear strain, the simple shear of 1% was applied along $[11\bar{2}]$ on the close-packed (111) plane (70). The effect of temperature on phase stability is derived from the volume- and temperature-dependent free energy computed by (71)

$$F(V, T) = E_0(V) + F_{\text{vib}}(V, T) + F_{\text{mag}}(V, T) - TS_{\text{conf}}$$

where $E_0(V)$ is the ground-state total energy, $F_{\text{vib}}(V, T)$ is the vibrational free energy, $F_{\text{mag}}(V, T)$ represents the contribution of magnetic excitation on the free energy, and S_{conf} is the configuration entropy. More calculation details can be found in (72).

Supplementary Materials

The PDF file includes:
 Supplementary Text
 Figs. S1 to S14
 Tables S1 to S3
 Legend for data S1
 References

Other Supplementary Material for this manuscript includes the following:

Data S1

REFERENCES AND NOTES

- B. Gludovatz, A. Hohenwarter, D. Catoor, E. H. Chang, E. P. George, R. O. Ritchie, A fracture-resistant high-entropy alloy for cryogenic applications. *Science* **345**, 1153–1158 (2014).
- B. Gludovatz, A. Hohenwarter, K. V. S. Thurston, H. Bei, Z. Wu, E. P. George, R. O. Ritchie, Exceptional damage-tolerance of a medium-entropy alloy CrCoNi at cryogenic temperatures. *Nat. Commun.* **7**, 10602 (2016).
- Y. H. Jo, S. Jung, W. M. Choi, S. S. Sohn, H. S. Kim, B. J. Lee, N. J. Kim, S. Lee, Cryogenic strength improvement by utilizing room-temperature deformation twinning in a partially recrystallized VCrMnFeCoNi high-entropy alloy. *Nat. Commun.* **8**, 15719 (2017).
- C. Lu, L. Niu, N. Chen, K. Jin, T. N. Yang, P. Xiu, Y. Zhang, F. Gao, H. Bei, S. Shi, M.-R. He, I. M. Robertson, W. J. Weber, L. M. Wang, Enhancing radiation tolerance by controlling defect mobility and migration pathways in multicomponent single-phase alloys. *Nat. Commun.* **7**, 13564 (2016).
- J. He, Q. Wang, H. Zhang, L. Dai, T. Mukai, Y. Wu, X. Liu, H. Wang, T.-G. Nieh, Z. Lu, Dynamic deformation behavior of a face-centered cubic FeCoNiCrMn high-entropy alloy. *Sci. Bull.* **63**, 362–368 (2018).
- D. Xu, M. Wang, T. Li, X. Wei, Y. Lu, A critical review of the mechanical properties of CoCrNi-based medium-entropy alloys. *Microstructures* **2**, 2022001 (2022).
- Z. An, S. Mao, Y. Liu, L. Yang, A. Vayyala, X. Wei, C. Liu, C. Shi, H. Jin, C. Liu, J. Zhang, Z. Zhang, X. Han, Inherent and multiple strain hardening imparting synergistic ultrahigh strength and ductility in a low stacking faulted heterogeneous high-entropy alloy. *Acta Mater.* **243**, 118516 (2023).
- Y. Tong, D. Chen, B. Han, J. Wang, R. Feng, T. Yang, C. Zhao, Y. L. Zhao, W. Guo, Y. Shimizu, C. T. Liu, P. K. Liaw, K. Inoue, Y. Nagai, A. Hu, J. J. Kai, Outstanding tensile properties of a precipitation-strengthened FeCoNiCrTi_{0.2} high-entropy alloy at room and cryogenic temperatures. *Acta Mater.* **165**, 228–240 (2019).
- Y. Shi, B. Yang, X. Xie, J. Brecht, K. A. Dahmen, P. K. Liaw, Corrosion of Al_xCoCrFeNi high-entropy alloys: Al-content and potential scan-rate dependent pitting behavior. *Corros. Sci.* **119**, 33–45 (2017).
- N. Xiao, X. Guan, D. Wang, H. Yan, M. Cai, N. Jia, Y. Zhang, C. Esling, X. Zhao, L. Zuo, Impact of W alloying on microstructure, mechanical property and corrosion resistance of face-centered cubic high entropy alloys. *Int. J. Miner. Metall. Mater.* **30**, 1667–1679 (2023).
- S. J. Sun, Y. Z. Tian, X. H. An, H. R. Lin, J. W. Wang, Z. F. Zhang, Ultrahigh cryogenic strength and exceptional ductility in ultrafine-grained CoCrFeMnNi high-entropy alloy with fully recrystallized structure. *Mater. Today Nano* **4**, 46–53 (2018).
- W. Han, Y. Liu, F. Wan, P. Liu, X. Yi, Q. Zhan, D. Morrall, S. Ohnuki, Deformation behavior of austenitic stainless steel at deep cryogenic temperatures. *J. Nucl. Mater.* **504**, 29–32 (2018).
- R. Ortwein, B. Skoczeń, J. P. Tock, Micromechanics based constitutive modeling of martensitic transformation in metastable materials subjected to torsion at cryogenic temperatures. *Int. J. Plast.* **59**, 152–179 (2014).
- Z. Li, K. G. Pradeep, Y. Deng, D. Raabe, C. C. Tasan, Metastable high-entropy dual-phase alloys overcome the strength-ductility trade-off. *Nature* **534**, 227–230 (2016).

15. J. Su, D. Raabe, Z. Li, Hierarchical microstructure design to tune the mechanical behavior of an interstitial TRIP-TWIP high-entropy alloy. *Acta Mater.* **163**, 40–54 (2019).
16. Z. Li, C. C. Tasan, H. Springer, B. Gault, D. Raabe, Interstitial atoms enable joint twinning and transformation induced plasticity in strong and ductile high-entropy alloys. *Sci. Rep.* **7**, 40704 (2017).
17. W. Zhang, D. Yan, W. Lu, Z. Li, Carbon and nitrogen co-doping enhances phase stability and mechanical properties of a metastable high-entropy alloy. *J. Alloys Compd.* **831**, 154799 (2020).
18. Y. Han, H. Li, H. Feng, K. Li, Y. Tian, Z. Jiang, Simultaneous enhancement in strength and ductility of $\text{Fe}_{50}\text{Mn}_{30}\text{Co}_{10}\text{Cr}_{10}$ high-entropy alloy via nitrogen alloying. *J. Mater. Sci. Technol.* **65**, 210–215 (2021).
19. Z. He, N. Jia, H. Wang, H. Yan, Y. Shen, Synergy effect of multi-strengthening mechanisms in FeMnCoCrN HEA at cryogenic temperature. *J. Mater. Sci. Technol.* **86**, 158–170 (2021).
20. J. Ding, Q. Yu, M. Asta, R. O. Ritchie, Tunable stacking fault energies by tailoring local chemical order in CrCoNi medium-entropy alloys. *Proc. Natl. Acad. Sci. U.S.A.* **115**, 8919–8924 (2018).
21. Q. Ding, Y. Zhang, X. Chen, X. Fu, D. Chen, S. Chen, L. Gu, F. Wei, H. Bei, Y. Gao, M. R. Wen, J. X. Li, Z. Zhang, T. Zhu, R. O. Ritchie, Q. Yu, Tuning element distribution, structure and properties by composition in high-entropy alloys. *Nature* **574**, 223–227 (2019).
22. R. Zhang, S. Zhao, J. Ding, Y. Chong, T. Jia, C. Ophus, M. Asta, R. O. Ritchie, A. M. Minor, Short-range order and its impact on the CrCoNi medium-entropy alloy. *Nature* **581**, 283–287 (2020).
23. X. Chen, Q. Wang, Z. Cheng, M. Zhu, H. Zhou, P. Jiang, L. Zhou, Q. Xue, F. Yuan, J. Zhu, X. Wu, E. Ma, Direct observation of chemical short-range order in a medium-entropy alloy. *Nature* **592**, 712–716 (2021).
24. L. Zhou, Q. Wang, J. Wang, X. Chen, P. Jiang, H. Zhou, F. Yuan, X. Wu, Z. Cheng, E. Ma, Atomic-scale evidence of chemical short-range order in CrCoNi medium-entropy alloy. *Acta Mater.* **224**, 117490 (2022).
25. X. Chen, F. Yuan, H. Zhou, X. Wu, Structure motif of chemical short-range order in a medium-entropy alloy. *Mater. Res. Lett.* **10**, 149–155 (2022).
26. M. Sudmanns, J. A. El-Awady, The effect of local chemical ordering on dislocation activity in multi-principle element alloys: A three-dimensional discrete dislocation dynamics study. *Acta Mater.* **220**, 117307 (2021).
27. Q.-J. Li, H. Sheng, E. Ma, Strengthening in multi-principal element alloys with local-chemical-order roughened dislocation pathways. *Nat. Commun.* **10**, 3563 (2019).
28. J. B. Seol, J. W. Bae, J. G. Kim, H. Sung, Z. Li, H. H. Lee, S. H. Shim, J. H. Jang, W. S. Ko, S. I. Hong, H. S. Kim, Short-range order strengthening in boron-doped high-entropy alloys for cryogenic applications. *Acta Mater.* **194**, 366–377 (2020).
29. J. Wang, P. Jiang, F. Yuan, X. Wu, Chemical medium-range order in a medium-entropy alloy. *Nat. Commun.* **13**, 1021 (2022).
30. L. Li, Z. Chen, S. Kuroiwa, M. Ito, K. Yuge, K. Kishida, H. Tanimoto, Y. Yu, H. Inui, E. P. George, Evolution of short-range order and its effects on the plastic deformation behavior of single crystals of the equiatomic Cr-Co-Ni medium-entropy alloy. *Acta Mater.* **243**, 118537 (2023).
31. Y. Liu, H. Zhang, Y. Yang, L. Sun, X. Zhao, H.-L. Yan, Y. Shen, N. Jia, Chemical short-range order dependence of micromechanical behavior in CoCrNi medium-entropy alloy studied by atomic simulations. *J. Alloys Compd.* **968**, 172002 (2023).
32. Z. He, N. Jia, H. Yan, Y. Shen, M. Zhu, X. Guan, X. Zhao, S. Jin, G. Sha, Y. Zhu, C. T. Liu, Multi-heterostructure and mechanical properties of N-doped FeMnCoCr high entropy alloy. *Int. J. Plast.* **139**, 102965 (2021).
33. E. El-Danaf, S. R. Kalidindi, R. D. Doherty, Influence of grain size and stacking-fault energy on deformation twinning in fcc metals. *Metall. Mater. Trans. A* **30**, 1223–1233 (1999).
34. M. J. Sohrabi, H. Mirzadeh, S. Sadeghpour, R. Mahmudi, Grain size dependent mechanical behavior and TRIP effect in a metastable austenitic stainless steel. *Int. J. Plast.* **160**, 103502 (2023).
35. J. M. Robinson, M. P. Shaw, Microstructural and mechanical influences on dynamic strain aging phenomena. *Int. Mater. Rev.* **39**, 113–122 (1994).
36. N. Jia, Y. D. Wang, S. D. Wu, W. Z. Han, Y. N. Wang, J. N. Deng, P. K. Liaw, Anomalous hardening in copper due to the growth of deformation-induced micro-twins after annealing. *Scr. Mater.* **54**, 1247–1252 (2006).
37. Z. He, Y. Guo, L. Sun, H.-L. Yan, X. Guan, S. Jiang, Y. Shen, W. Yin, X. Zhao, Z. Li, N. Jia, Interstitial-driven local chemical order enables ultrastrong face-centered cubic multicomponent alloys. *Acta Mater.* **243**, 118495 (2023).
38. R. L. Fullman, Measurement of particle sizes in opaque bodies. *JOM* **5**, 447–452 (1953).
39. S. Mahajan, C. S. Pande, M. A. Imam, B. B. Rath, Formation of annealing twins in f.c.c. crystals. *Acta Mater.* **45**, 2633–2638 (1997).
40. S. L. Wong, M. Madivala, U. Prahla, F. Roters, D. Raabe, A crystal plasticity model for twinning- and transformation-induced plasticity. *Acta Mater.* **118**, 140–151 (2016).
41. T. Ungár, J. Gubicza, G. Ribárik, A. Borbély, Crystallite size distribution and dislocation structure determined by diffraction profile analysis: Principles and practical application to cubic and hexagonal crystals. *J. Appl. Cryst.* **34**, 298–310 (2001).
42. B. Zhao, P. Huang, L. Zhang, S. Li, Z. Zhang, Q. Yu, Temperature effect on stacking fault energy and deformation mechanisms in titanium and titanium-aluminium alloy. *Sci. Rep.* **10**, 3086 (2020).
43. I. Basu, J. T. M. De Hosson, Strengthening mechanisms in high entropy alloys: Fundamental issues. *Scr. Mater.* **187**, 148–156 (2020).
44. K. Biswas, J.-W. Yeh, P. P. Bhattacharjee, J. T. M. De Hosson, High entropy alloys: Key issues under passionate debate. *Scr. Mater.* **188**, 54–58 (2020).
45. Q. Ding, X. Fu, D. Chen, H. Bei, B. Gludovatz, J. Li, Z. Zhang, E. P. George, Q. Yu, T. Zhu, R. O. Ritchie, Real-time nanoscale observation of deformation mechanisms in CrCoNi -based medium- to high-entropy alloys at cryogenic temperatures. *Mater. Today* **25**, 21–27 (2019).
46. Y. J. Zhang, D. Han, X. W. Li, A unique two-stage strength-ductility match in low solid-solution hardening Ni-Cr alloys: Decisive role of short range ordering. *Scr. Mater.* **178**, 269–273 (2020).
47. S. Chen, Z. H. Aitken, S. Pattamatta, Z. Wu, Z. G. Yu, D. J. Srolovitz, P. K. Liaw, Y.-W. Zhang, Short-range ordering alters the dislocation nucleation and propagation in refractory high-entropy alloys. *Mater. Today* **65**, 14–25 (2023).
48. S. Lee, M. J. Duarte, M. Feuerbacher, R. Soler, C. Kirchlechner, C. H. Liebscher, S. H. Oh, G. Dehm, Dislocation plasticity in FeCoCrMnNi high-entropy alloy: Quantitative insights from *in situ* transmission electron microscopy deformation. *Mater. Res. Lett.* **8**, 216–224 (2020).
49. D. B. Williams, C. B. Carter, *Transmission Electron Microscopy* (Springer, 2009).
50. Y. F. Shen, N. Jia, Y. D. Wang, X. Sun, L. Zuo, D. Raabe, Suppression of twinning and phase transformation in an ultrafine grained 2 GPa strong metastable austenitic steel: Experiment and simulation. *Acta Mater.* **97**, 305–315 (2015).
51. M. Naeem, H. He, F. Zhang, H. Huang, S. Harjo, T. Kawasaki, B. Wang, S. Lan, Z. Wu, F. Wang, Y. Wu, Z. Lu, Z. Zhang, C. T. Liu, X.-L. Wang, Cooperative deformation in high-entropy alloys at ultralow temperatures. *Sci. Adv.* **6**, eaax4002 (2020).
52. H.-F. Zhang, H.-L. Yan, F. Fang, N. Jia, Reverse transformation in [110]-oriented face-centered-cubic single crystals studied by atomic simulations. *Acta Metall. Sin.* **35**, 1631–1640 (2022).
53. P. Wu, Y. Zhang, L. Han, K. Gan, D. Yan, W. Wu, L. He, Z. Fu, Z. Li, Unexpected sluggish martensitic transformation in a strong and super-ductile high-entropy alloy of ultralow stacking fault energy. *Acta Mater.* **261**, 119389 (2023).
54. L. Guo, J. Gu, X. Gong, K. Li, S. Ni, Y. Liu, M. Song, Short-range ordering induced serrated flow in a carbon contained FeCoCrNiMn high entropy alloy. *Micron* **126**, 102739 (2019).
55. Z. Lei, X. Liu, Y. Wu, H. Wang, S. Jiang, S. Wang, X. Hui, Y. Wu, B. Gault, P. Kontis, D. Raabe, L. Gu, Q. Zhang, H. Chen, H. Wang, J. B. Liu, K. An, Q. Zeng, T.-G. Nieh, Z. Lu, Enhanced strength and ductility in a high-entropy alloy via ordered oxygen complexes. *Nature* **563**, 546–550 (2018).
56. D. Utt, S. Lee, Y. L. Xing, H. Jeong, A. Stukowski, S. H. Oh, G. Dehm, K. Albe, The origin of jerky dislocation motion in high-entropy alloys. *Nat. Commun.* **13**, 4777 (2022).
57. P. Cao, Maximum strength and dislocation patterning in multi-principle element alloys. *Sci. Adv.* **8**, eabq7433 (2022).
58. T. M. Smith, M. S. Hooshmand, B. D. Esser, F. Otto, D. W. McComb, E. P. George, M. Ghazisaeidi, M. J. Mills, Atomic-scale characterization and modeling of 60° dislocations in a high-entropy alloy. *Acta Mater.* **110**, 352–363 (2016).
59. Y. L. Zhao, Y. R. Li, G. M. Yeli, J. H. Luan, S. F. Liu, W. T. Lin, D. Chen, X. J. Liu, J. J. Kai, C. T. Liu, T. Yang, Anomalous precipitate-size-dependent ductility in multicomponent high-entropy alloys with dense nanoscale precipitates. *Acta Mater.* **223**, 117480 (2022).
60. L. Wang, J. Ding, S. Chen, K. Jin, Q. Zhang, J. Cui, B. Wang, B. Chen, T. Li, Y. Ren, S. Zheng, K. Ming, W. Lu, J. Hou, G. Sha, J. Liang, L. Wang, Y. Xue, E. Ma, Tailoring planar slip to achieve pure metal-like ductility in body-centred-cubic multi-principle element alloys. *Nat. Mater.* **22**, 950–957 (2023).
61. M. Niewczas, Z. S. Basinski, S. J. Basinski, J. D. Embury, Deformation of copper single crystals to large strains at 4.2K. *Philos. Mag. A* **81**, 1121–1142 (2001).
62. X. R. Guo, C. Y. Sun, R. Li, N. Guo, Y. C. Wei, Z. X. Su, S. P. Yan, A dislocation density based model for twinning induced softening of TWIP steel. *Comput. Mater. Sci.* **139**, 8–15 (2017).
63. T. Yang, W. Wen, G. Z. Yin, X. L. Li, M. Gao, Y. L. Gu, L. Li, Y. Liu, H. Lin, X. M. Zhang, B. Zhao, T. K. Liu, Y. G. Yang, Z. Li, X. T. Zhou, X. Y. Gao, Introduction of the X-ray diffraction beamline at SSRF. *Nucl. Sci. Tech.* **26**, 020101 (2015).
64. L. Vitos, Total-energy method based on the exact muffin-tin orbitals theory. *Phys. Rev. B* **64**, 014107 (2001).
65. L. Vitos, *Computational Quantum Mechanics for Materials Engineers: The EMTO Method and Applications* (Springer, 2007).
66. S. Huang, X. Li, H. Huang, E. Holmström, L. Vitos, Mechanical performance of FeCrCoMnAl_x high-entropy alloys from first-principle. *Mater. Chem. Phys.* **210**, 37–42 (2018).
67. J. Perdew, K. Burke, M. Ernzerhof, Generalized gradient approximation made simple. *Phys. Rev. Lett.* **77**, 3865–3868 (1996).
68. H. F. Zhang, H. L. Yan, H. Yu, Z. W. Ji, Q. M. Hu, N. Jia, The effect of Co and Cr substitutions for Ni on mechanical properties and plastic deformation mechanism of FeMnCoCrNi high entropy alloys. *J. Mater. Sci. Technol.* **48**, 146–155 (2020).

69. H. Huang, X. Li, Z. Dong, W. Li, S. Huang, D. Meng, X. Lai, T. Liu, S. Zhu, L. Vitos, Critical stress for twinning nucleation in CrCoNi-based medium and high entropy alloys. *Acta Mater.* **149**, 388–396 (2018).
70. X. Li, S. Schonecker, W. Li, L. K. Varga, D. L. Irving, L. Vitos, Tensile and shear loading of four fcc high-entropy alloys: A first-principles study. *Phys. Rev. B* **97**, 094102 (2018).
71. D. Ma, B. Grabowski, F. Körmann, J. Neugebauer, D. Raabe, *Ab initio* thermodynamics of the CoCrFeMnNi high entropy alloy: Importance of entropy contributions beyond the configurational one. *Acta Mater.* **100**, 90–97 (2015).
72. Y.-X. Guo, H.-L. Yan, N. Jia, B. Yang, Z. Li, L. Zuo, Correlations between valence electron concentration and the phase stability, intrinsic strength, and deformation mechanism in fcc multicomponent alloys. *Phys. Rev. B* **109**, 004100 (2024).
73. S. Jiang, R. L. Peng, Z. Hegedűs, T. Gnäupel-Herold, J. J. Moverare, U. Lienert, F. Fang, X. Zhao, L. Zuo, N. Jia, Micromechanical behavior of multilayered Ti/Nb composites processed by accumulative roll bonding: An in-situ synchrotron X-ray diffraction investigation. *Acta Mater.* **205**, 116546 (2021).
74. F. HajyAkbary, J. Sietsma, A. J. Böttger, M. J. Santofimia, An improved X-ray diffraction analysis method to characterize dislocation density in lath martensitic structures. *Mater. Sci. Eng. A* **639**, 208–218 (2015).
75. T. Ungár, I. Dragomir, Á. Révész, A. Borbély, The contrast factors of dislocations in cubic crystals: The dislocation model of strain anisotropy in practice. *J. Appl. Cryst.* **32**, 992–1002 (1999).
76. W. Li, D. Xie, D. Li, Y. Zhang, Y. Gao, P. K. Liaw, Mechanical behavior of high-entropy alloys. *Prog. Mater. Sci.* **118**, 100777 (2021).

Acknowledgments: We thank N. Zhang and Y. Dong at the Analytical and Testing Center of Northeastern University for the assistance with EBSD and TEM characterizations, and T. He and Y.Q. Yang for the support on texture measurements. The present work has also benefited from the BL14B1 beamline at the SSRF. **Funding:** We acknowledge the financial support from the National Natural Science Foundation of China (nos. 52371097, 52301135, and 51922026) and the Fundamental Research Funds for the Central Universities (no. N2325029). P.K.L. appreciates the support from the NSF (DMR-1611180, 1809640, and 2226508) and the Army Research Office (W911NF-13-1-0438 and W911NF-19-2-0049). **Author contributions:** N.J. and Z.H. conceived the idea and supervised the project. L.S. prepared materials and conducted mechanical testing. L.S. and Z.H. performed HEXRD and SEM. X.G. conducted TEM characterizations. S.J. processed HEXRD data. Y.G. and H.-L.Y. performed first-principles calculation based on DFT. L.S., Z.H., N.J., Y.Y., Y.L., Y.S., H.-L.Y., and P.K.L. analyzed the data and discussed the results. L.S., Z.H., and N.J. wrote the manuscript. All authors reviewed and contributed to the final manuscript. **Competing interests:** The authors declare that they have no known competing financial interests or personal relationships that could have appeared to influence the work reported in this paper. **Data and materials availability:** All data needed to evaluate the conclusions in this paper are present in the paper and/or the Supplementary Materials.

Submitted 11 June 2024

Accepted 25 October 2024

Published 29 November 2024

10.1126/sciadv.adq6398